Selecting Suitable Coherent Processing Time Window Lengths for Ground-Based ISAR Imaging of Cooperative Sea Vessels

M. Y. Abdul Gaffar, W. A. J. Nel, and M. R. Inggs

***Abstract*—Inverse synthetic aperture radar (ISAR) imaging of sea vessels is a challenging task because their 3-D rotational motion over the coherent processing interval (CPI) often leads to blurred images. The selection of the duration of the CPI, also known as the coherent processing time window length (CPTWL), is critical because it should be short enough to limit the blurring caused by the 3-D rotational motion and long enough to ensure that the desired cross-range resolution is obtained. This paper proposes an algorithm, referred to as the motion-aided CPTWL selector (MACS) algorithm, which selects suitable CPTWLs for ISAR imaging of cooperative sea vessels. The suggested CPTWLs may be used to obtain motion-compensated ISAR images that have the desired medium cross-range resolution and limited blurring due to 3-D rotational motion. The proposed algorithm is applied to measured motion data of three different classes of sea vessels: a yacht, a fishing trawler, and a survey vessel. Results show that longer CPTWLs are needed for larger vessels in order to obtain ISAR images with the desired cross-range resolution. The effectiveness of the CPTWLs, suggested by the MACS algorithm, is shown using measured radar data. The suggested CPTWLs may also be used to select an effective initial CPTWL for Martorella/Berizzi's optimum imaging selection algorithm when it is applied to measured radar data of small vessels. Lastly, the proposed technique offers significant computational savings for radar cross section measurement applications where a few high-quality ISAR images are desired from long radar recordings.**

***Index Terms*—Coherent processing time window lengths (CPTWLs), inverse synthetic aperture radar (ISAR), radar cross section (RCS) measurement, sea vessels.**

I. Introduction

INVERSE synthetic aperture radar (ISAR) images of objects have been shown to contain valuable information for a wide range of military applications such as radar cross section (RCS) measurement [1] and noncooperative target recognition [2]–[4]. RCS measurement of military objects (fighter aircraft and warships) is important, since it helps to identify the scattering centers of high reflectivity that require RCS reduction for stealth purposes. This process is able to identify physical features of the platform that lead to significant RCS contributions such as nonoptimal placement of antennas on the upper deck of a ship. Reducing the absolute RCS of a ship can provide the advantage of reducing the acquisition range of an antiship missile as well as improving the performance of a ship's countermeasure against the approaching seeker.

The ISAR imaging process uses the rotational motion of an object to provide cross-range information. It operates on the principle that scatterers on either side of a rotating object have different radial velocities with respect to the radar. Thus, cross-range information can be obtained by simply separating scatterers according to their Doppler frequency, as described by Wehner [5]. ISAR imaging of maritime vessels is a challenging task because their 3-D rotational motion (roll, pitch, and yaw rates) causes a continuously changing image projection plane, as shown by Chen and Miceli [6], Chen and Lipps [7], and Bao *et al.* [8]. Furthermore, the ISAR image of a maritime vessel may become distorted due to multipath and nonpointlike scattering mechanisms. Assuming a vessel's motion is the only cause of blurring, a focused cross-range-scaled ISAR image may be obtained using existing range alignment [9]–[11], autofocus [3], [12], [13], polar reformatting [14], [15], and cross-range scaling [16] algorithms. However, all these algorithms assume that a vessel's Doppler generating axis of rotation is constant over the coherent processing interval (CPI). When this assumption is not satisfied, the motion-compensated ISAR image is the sum of the object's projection onto the different image projection planes, and this may give rise to significant blurring, as shown by Abdul Gaffar and Nel [17].

Little work has been published on choosing the time duration of the CPI, referred to as the coherent processing time window length (CPTWL), which would minimize the blurring caused by a vessel's 3-D rotational motion. If the CPTWL is too short, the desired cross-range resolution may not be achieved. Conversely, if the CPTWL is too long, the 3-D rotational motion of the vessel causes blurring in the ISAR image. It is reported in [5] that the optimum CPTWL for unfocused ISAR lies between 0.025 and 0.5 s for X-band measurements of ships. However, this paper gives no information on how this suggested range of CPTWLs changes for different classes of sea vessels and sea conditions. In addition, the suggested range is too broad, as it spans more than an order of magnitude. An optimum imaging selection algorithm was proposed by Martorella and Berizzi [18] to estimate the optimum central instant of the processing interval as well as the optimum CPTWL that provides an ISAR image with the highest focus. However, Martorella/Berizzi's algorithm does not show how to chose the initial CPTWL for a specific radar data set, and the suitability of this technique for small ships with chaotic motion has not been investigated.

Manuscript received September 12, 2008; revised January 20, 2009. First published June 5, 2009; current version published August 28, 2009. This work was supported in part by the South African Department of Defence and in part by the South African Department of Science and Technology.

M. Y. Abdul Gaffar and W. A. J. Nel are with the Council for Scientific and Industrial Research, Radar and Electronic Warfare, Pretoria 0001, South Africa.

M. R. Inggs is with the Department of Electrical Engineering, University of Cape Town, Rondebosch 7701, South Africa.

Digital Object Identifier 10.1109/TGRS.2009.2019729

Moreover, it does not take advantage of motion data from instrumented vessels that may be available during measurements trials for RCS measurement purposes.

This paper proposes a new technique, referred to as motion-aided CPTWL selector (MACS), which suggests suitable CPTWLs for ISAR imaging of cooperative sea vessels. The proposed technique takes advantage of the motion data of an instrumented vessel, and the suggested CPTWLs may be used to form ISAR images with medium cross-range resolution that has limited blurring due to the vessel's 3-D rotational motion. A good feature associated with the MACS algorithm is that the suggested range of suitable CPTWLs is much smaller than that reported in [5]. In addition, the proposed technique can be used to select an effective initial CPTWL for Martorella/Berizzi's optimum imaging selection algorithm proposed in [18], when it is applied to measured radar data of small vessels. Experimental results obtained from applying the MACS algorithm to motion data of three different classes of vessels (a yacht, a fishing trawler, and a survey vessel) have shown that suitable CPTWLs are dependent on the class of the vessel. The effectiveness of the suggested CPTWL is shown using real radar measurements of a yacht.

II. System Model

We denote a quaternion $\mathbf{q}_x(\mathbf{h},\theta)$, arbitrarily labeled x, representing a rotation through an angle θ about an axis $\mathbf{h} = [\,h_1 \quad h_2 \quad h_3\,]$ in vector form as

$$\mathbf{q}_x(\mathbf{h},\theta) = \left[\cos\left(\frac{\theta}{2}\right)\ \mathbf{h}\sin\left(\frac{\theta}{2}\right)\right] \tag{1}$$

or in scalar form[1]

$$\mathbf{q}_x(\mathbf{h},\theta) = \left[q_x^{\{1\}} \quad q_x^{\{2\}} \quad q_x^{\{3\}} \quad q_x^{\{4\}}\right]. \tag{2}$$

More details about using quaternions to represent rotations can be found in [19]. The system model considers a vessel with only rotational motion and assumes that any translation motion has been compensated. Two coordinate axes are defined (see Fig. 1): the radar coordinate axes (U,V,W), which are fixed and the vessel's coordinate axes (X_n,Y_n,Z_n), which change as the vessel experiences 3-D rotational motion. In this diagram, $R_{k,t(n)}$ denotes the distance from the radar to the kth scatterer of the vessel for time $t(n)$ and R_0 represents the distance from the radar to the vessel's center of rotation.

The 4-D quaternion representation of the local coordinates of the kth scatterer is expressed as $\mathbf{q}_{rk} = [\,0 \quad \mathbf{r}_k\,]$, where $\mathbf{r}_k = [\,x_k \quad y_k \quad z_k\,]$. However, it is the global coordinates of the kth scatterer, denoted by $\mathbf{g}_{k,t(n)} = [\,u_{k,t(n)} \quad v_{k,t(n)} \quad w_{k,t(n)}\,]$, which is needed to calculate the phase at the radar receiver. Assume that the radar continuously tracks the vessel so that the vessel's center of rotation always lies on the global U axis, and the physical dimensions of the vessel are much less than R_0. Then, the global coordinates of the kth scatterer at $t(n)$, which

[1]It should be noted that the superscripts $\{1\}$, $\{2\}$, $\{3\}$, and $\{4\}$ are used to denote the respective scalar elements of the quaternion.

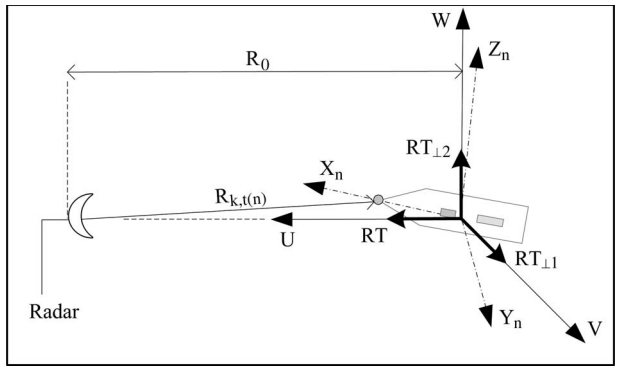

Fig. 1. System model of the radar and the vessel showing the global and local coordinate axes.

is denoted by $\mathbf{q}_{gk,t(n)}$ in 4-D quaternion notation and $\mathbf{g}_{k,t(n)}$ in 3-D form, can be expressed as

$$\mathbf{q}_{gk,t(n)} = (\mathbf{q}_{\mathrm{tot},\Delta t(n)})^* \otimes \left((\mathbf{q}_{\mathrm{ins},t(n-1)})^* \otimes \mathbf{q}_{rk} \otimes (\mathbf{q}_{\mathrm{ins},t(n-1)})\right) \otimes (\mathbf{q}_{\mathrm{tot},\Delta t(n)}) \tag{3}$$

$$\mathbf{g}_{k,t(n)} = \left[q_{gk,t(n)}^{\{2\}} \quad q_{gk,t(n)}^{\{3\}} \quad q_{gk,t(n)}^{\{4\}}\right] \tag{4}$$

where $*$ denotes the complex conjugate operation, $\otimes$ represents quaternion multiplication, $\mathbf{q}_{\mathrm{ins},t(n-1)}$ is the unit quaternion that represents the combined 3-D rotation of heading $\theta_{\mathrm{hs},t(n-1)}$, elevation $\theta_{\mathrm{e},t(n-1)}$, and bank $\theta_{\mathrm{b},t(n-1)}$ for time $t(n-1)$, and $\mathbf{q}_{\mathrm{tot},\Delta t(n)}$ is a unit quaternion that denotes the vessel's incremental rotational motion over $\Delta t(n)$. Stated mathematically

$$\begin{aligned}\mathbf{q}_{\mathrm{ins},t(n-1)} = {} & \mathbf{q}_{\mathrm{hs},t(n-1)}(\mathbf{RT}_{\perp 2},\theta_{\mathrm{hs},t(n-1)}) \\ & \otimes \mathbf{q}_{\mathrm{e},t(n-1)}(\mathbf{RT}_{\perp 1},\theta_{\mathrm{e},t(n-1)}) \\ & \otimes \mathbf{q}_{\mathrm{b},t(n-1)}(\mathbf{RT},\theta_{\mathrm{b},t(n-1)})\end{aligned} \tag{5}$$

$$\begin{aligned}\mathbf{q}_{\mathrm{tot},\Delta t(n)} = {} & \mathbf{q}_{\mathrm{y},\Delta t(n)}(\mathbf{z}_n,\theta_{\mathrm{y},\Delta t(n)}) \\ & \otimes \mathbf{q}_{\mathrm{p},\Delta t(n)}(\mathbf{y}_n,\theta_{\mathrm{p},\Delta t(n)}) \\ & \otimes \mathbf{q}_{r,\Delta t(n)}(\mathbf{x}_n,\theta_{\mathrm{r},\Delta t(n)})\end{aligned} \tag{6}$$

where the unit vectors $\mathbf{z}_n$, $\mathbf{y}_n$, and $\mathbf{x}_n$ are defined about the local coordinate axes X_n, Y_n, and Z_n, respectively; the unit vectors $\mathbf{RT} = [\,1 \quad 0 \quad 0\,]$, $\mathbf{RT}_{\perp 1} = [\,0 \quad 1 \quad 0\,]$, and $\mathbf{RT}_{\perp 2} = [\,0 \quad 0 \quad 1\,]$ are unit vectors about the U, V, and W axes, respectively. The heading $\theta_{\mathrm{hs},t(n-1)}$, elevation $\theta_{\mathrm{e},t(n-1)}$, and bank $\theta_{\mathrm{b},t(n-1)}$ angles define the orientation of the vessel at $t(n-1)$, and the yaw $\theta_{\mathrm{y},\Delta t(n)}$, pitch $\theta_{\mathrm{p},\Delta t(n)}$, and roll $\theta_{\mathrm{r},\Delta t(n)}$ angles represent the nth incremental rotational motion about a vessel's local axes, which corresponds to the convention adopted in [19]. In this system model, the rotational sequence is assumed to be heading, elevation and then bank.

Assume that a vessel can be represented by K point scatterers, then the received signal at the radar is made up of the contributions from all the scatterers. The phase of the received signal at time $t(n)$ is dependent on the range of the kth scatterer $R_{k,t(n)}$, which can be expressed in terms of the global coordinates $\mathbf{g}_{k,t(n)}$

$$R_{k,t(n)} = \sqrt{(R_0 - u_{k,t(n)})^2 + (v_{k,t(n)})^2 + (w_{k,t(n)})^2}. \tag{7}$$

Further assume that the radar transmits a stepped frequency waveform and that the motion of the vessel is stationary over the burst.[2] Then, the signal received by the radar $\Phi(n,m)$ is given by

$$\Phi(n,m) = \alpha_k \sum_{k=1}^{K} e^{\left(-j2\pi f_{c,m}\frac{2R_{k,t(n)}}{c}\right)} + e(n,m) \quad (8)$$

where $f_{c,m}$ represents the center frequency of mth transmitted pulse within a burst, and a burst of M pulses is compressed to form a high range resolution (HRR) profile, n represents the burst number, α_k is the RCS of the kth scatterer, c is the speed of light, and $e(n,m)$ denotes the clutter and noise.

The system model presented in this paper is different to the other models found in the ISAR literature, and it is useful in the following ways.

1) The vessel's current aspect, denoted by $(\mathbf{q}_{\text{ins},t(n-1)}\mathbf{q}_{rk}(\mathbf{q}_{\text{ins},t(n-1)})^*)$, and its incremental rotational motion over a discrete rotation, expressed by $\mathbf{q}_{\text{tot},\Delta t(n)}$, are clearly expressed in (3). The variation of these two parameters over the CPI can be used to predict the presentation[3] of a vessel.
2) The incremental rotational motion of a vessel between discrete rotations $\mathbf{q}_{\text{tot},\Delta t(n)}$ can be used to calculate the vessel's image-generating Doppler components, which consist of the Doppler generating axis of rotation and the effective angular rotation rate, as shown by the transformation proposed by Abdul Gaffar *et al.* [20]. This information can be used to explain the blurring caused by 3-D rotational motion [17] as well as to assess the degree of 3-D rotational motion that exists in a CPI [20]. Furthermore, it is an essential tool for the proposed MACS algorithm, and a short summary of the transformation is given in the next section.
3) The system model that is proposed is flexible enough to accept 3-D rotational motion measured from an attitude sensor. Thus, it can be used to develop a point-scatterer ISAR simulation that incorporates realistic motion.

III. Extraction of the Image-Generating Doppler for ISAR

It is well known in the literature that the Doppler-generating axis of rotation influences the presentation of a vessel in the ISAR image, and that the effective angular rotation rate is used to obtain the predicted cross-range resolution [6]. The effect of a time-varying Doppler generating axis of rotation, and the effective angular rotation rate was characterized separately by Abdul Gaffar and Nel [17] and Wong *et al.* [21], respectively. It was shown that these two time-varying parameters may give rise to blurring in the ISAR image. For this reason, it is important to extract these parameters from measured motion data so that the causes of blurring due to 3-D rotational motion can be well understood.

[2]This implies that the distance traversed by an object over an ISAR burst is much less than the down-range resolution of the high range resolution profile. This assumption is valid for imaging sailing yachts with a typical speed of 6 kn and a medium resolution of 0.5 m, when the burst repetition frequency is greater than 100 Hz.

[3]Presentation refers to the orientation of a vessel in an ISAR image, as defined by Musman et al [2].

The transformation proposed in [20] extracts the image-generating Doppler components from measured motion data. The transformation is made up of the following processing steps.

1) Obtain the heading $\theta_{\text{hs},t(n)}$ used in the system model

$$\theta_{\text{hs},t(n)} = \text{mod}(180^\circ + \theta_{\text{h},t(n)} - \theta_{\text{b},t(n)}, 360^\circ) \quad (9)$$

where $\text{mod}(a,b)$ is the modulus operation of a with b, $\theta_{\text{b},t(n)}$ denotes the bearing of the vessel obtained from GPS position data, and $\theta_{\text{h},t(n)}$ represents the heading measured from an inertial navigation system. The heading that is used in the system model is defined such that $\theta_{\text{hs},t(n)}$ is zero when the vessel is sailing directly inbound to the radar, and it increases positively as the vessel rotates clockwise.
2) Calculate the quaternion $\mathbf{q}_{\text{tot},\Delta t(n)}$ that represents the vessel's incremental rotational motion over the discrete interval $\Delta t(n)$

$$\begin{aligned}\mathbf{q}_{\text{tot},\Delta t(n)} = {} & \mathbf{q}_{\text{b},t(n-1)}(\mathbf{RT}, -\theta_{\text{b},t(n-1)}) \\ & \otimes \mathbf{q}_{\text{e},t(n-1)}(\mathbf{RT}_{\perp 1}, -\theta_{\text{e},t(n-1)}) \\ & \otimes \mathbf{q}_{\text{hs},t(n-1)}(\mathbf{RT}_{\perp 2}, -\theta_{\text{hs},t(n-1)}) \\ & \otimes \mathbf{q}_{\text{hs},t(n)}(\mathbf{RT}_{\perp 2}, \theta_{\text{hs},t(n)}) \\ & \otimes \mathbf{q}_{\text{e},t(n)}(\mathbf{RT}_{\perp 1}, \theta_{\text{e},t(n)}) \\ & \otimes \mathbf{q}_{\text{b},t(n)}(\mathbf{RT}, \theta_{\text{b},t(n)}). \end{aligned} \quad (10)$$

3) The quaternion $\mathbf{q}_{\text{tot},\Delta t(n)}$ is used to obtain the effective roll angle $\theta_{\text{RT},\Delta t(n)}$ using

$$A_{\Delta t(n)} = q^{\{1\}}_{\text{tot},\Delta t(n)} q^{\{2\}}_{\text{tot},\Delta t(n)} + q^{\{3\}}_{\text{tot},\Delta t(n)} q^{\{4\}}_{\text{tot},\Delta t(n)} \quad (11)$$

$$B_{\Delta t(n)} = -\left(q^{\{1\}}_{\text{tot},\Delta t(n)}\right)^2 + \left(q^{\{3\}}_{\text{tot},\Delta t(n)}\right)^2 \quad (12)$$

$$D_{\Delta t(n)} = \left(q^{\{2\}}_{\text{tot},\Delta t(n)}\right)^2 - \left(q^{\{4\}}_{\text{tot},\Delta t(n)}\right)^2 \quad (13)$$

$$\theta_{\text{RT},\Delta t(n)} = \arctan\left(\frac{2A_{\Delta t(n)}}{-(B_{\Delta t(n)} + D_{\Delta t(n)})}\right). \quad (14)$$

4) Define the quaternion that represents the effective roll motion $\mathbf{q}_{\text{er},\Delta t(n)}$ as well as $s_{1,\Delta t(n)}$, $s_{2,\Delta t(n)}$, $s_{3,\Delta t(n)}$, and $s_{4,\Delta t(n)}$, which are used to obtain the effective pitch $\theta_{\text{RT}\perp 1,\Delta t(n)}$ and the effective yaw $\theta_{\text{RT}\perp 2,\Delta t(n)}$ angles

$$\begin{aligned}&\mathbf{q}_{\text{er},\Delta t(n)}\left(\mathbf{RT}, \theta_{\text{RT},\Delta t(n)}\right) \\ &\quad = \left[\cos\left(\frac{\theta_{\text{RT},\Delta t(n)}}{2}\right) \quad \mathbf{RT}\sin\left(\frac{\theta_{\text{RT},\Delta t(n)}}{2}\right)\right] \end{aligned} \quad (15)$$

$$\begin{aligned}&s_{1,\Delta t(n)} \\ &\quad = q^{\{1\}}_{\text{tot},\Delta t(n)} q^{\{1\}}_{\text{er},\Delta t(n)} + q^{\{2\}}_{\text{tot},\Delta t(n)} q^{\{2\}}_{\text{er},\Delta t(n)} \end{aligned} \quad (16)$$

$$\begin{aligned}&s_{2,\Delta t(n)} \\ &\quad = q^{\{2\}}_{\text{tot},\Delta t(n)} q^{\{1\}}_{\text{er},\Delta t(n)} - q^{\{1\}}_{\text{tot},\Delta t(n)} q^{\{2\}}_{\text{er},\Delta t(n)} \end{aligned} \quad (17)$$

$$s_{3,\Delta t(n)} = q^{\{3\}}_{\text{tot},\Delta t(n)} q^{\{1\}}_{\text{er},\Delta t(n)} - q^{\{4\}}_{\text{tot},\Delta t(n)} q^{\{2\}}_{\text{er},\Delta t(n)} \quad (18)$$

$$s_{4,\Delta t(n)} = q^{\{4\}}_{\text{tot},\Delta t(n)} q^{\{1\}}_{\text{er},\Delta t(n)} + q^{\{3\}}_{\text{tot},\Delta t(n)} q^{\{2\}}_{\text{er},\Delta t(n)}. \quad (19)$$

Calculate $\theta_{\mathrm{RT}\perp 1,\Delta t(n)}$ and $\theta_{\mathrm{RT}\perp 2,\Delta t(n)}$ angles as follows:

$$\theta_{\mathrm{RT}\perp 1,\Delta t(n)} = 2\arctan\left(\frac{s_{3,\Delta t(n)}}{s_{1,\Delta t(n)}}\right) \tag{20}$$

$$\theta_{\mathrm{RT}\perp 2,\Delta t(n)} = 2\arctan\left(\frac{s_{4,\Delta t(n)}}{s_{1,\Delta t(n)}}\right). \tag{21}$$

5) Obtain the Doppler generating motion represented by $\mathbf{q}_{\mathrm{eff},\Delta t(n)}$ using the effective pitch and yaw rotations

$$\begin{aligned}\mathbf{q}_{\mathrm{eff},\Delta t(n)}&(\mathbf{\Omega}_{\mathrm{eff},\Delta t(n)},\theta_{\mathrm{eff},\Delta t(n)})\\ &= \mathbf{q}_{\mathrm{ey},\Delta t(n)}(\mathbf{RT}_{\perp 2},\theta_{\mathrm{RT}\perp 2,\Delta t(n)})\\ &\quad\otimes \mathbf{q}_{\mathrm{ep},\Delta t(n)}(\mathbf{RT}_{\perp 1},\theta_{\mathrm{RT}\perp 1,\Delta t(n)})\end{aligned} \tag{22}$$

where $\mathbf{\Omega}_{\mathrm{eff},\Delta t(n)}$ and $\theta_{\mathrm{eff},\Delta t(n)}$ denotes the Doppler generating axis of rotation and the effective rotation angle, respectively.

6) Lastly, the effective angular rotation rate $\dot{\theta}_{\mathrm{eff},\Delta t(n)}$, the Doppler generating axis of rotation $\mathbf{\Omega}_{\mathrm{eff},\Delta t(n)}$, and the angle of the Doppler generating axis of rotation with respect to the V-axis denoted by $\theta_{\Omega\mathrm{eff}1,\Delta t(n)}$ can be obtained using the following equations:

$$\dot{\theta}_{\mathrm{eff},\Delta t(n)} = \frac{2\arccos\left(q^{\{1\}}_{\mathrm{eff},\Delta t(n)}\right)}{\Delta t(n)} \tag{23}$$

$$\mathbf{\Omega}_{\mathrm{eff},\Delta t(n)} = \frac{\left[q^{\{2\}}_{\mathrm{eff},\Delta t(n)} \quad q^{\{3\}}_{\mathrm{eff},\Delta t(n)} \quad q^{\{4\}}_{\mathrm{eff},\Delta t(n)}\right]}{\sin\left(\frac{\theta_{\mathrm{eff},\Delta t(n)}}{2}\right)} \tag{24}$$

$$\theta_{\Omega\mathrm{eff}1,\Delta t(n)} = \arctan 2\left(q^{\{4\}}_{\mathrm{eff},\Delta t(n)}, q^{\{3\}}_{\mathrm{eff},\Delta t(n)}\right) \tag{25}$$

where $\arctan 2$ is a two-argument function that computes the arctangent with a range of $(-180^\circ, 180^\circ]$.

The proposed MACS algorithm makes use of the transform described in this section to extract the image-generating Doppler components from measured motion data. It also considers the cross-range resolution error and the image blurring that is induced by these two time-varying parameters. The next section discusses this in more detail.

IV. Cross-Range Resolution

Cross-range resolution refers to the spatial length of each cross-range bin of an ISAR image after it is transformed from Doppler to distance. The cross-range dimension of an ISAR image fundamentally represents Doppler, and it can be transformed to distance under certain condition as explained in [5]. This section presents the derivation of the cross-range resolution, to highlight the assumptions that are made about the motion of an object.

Fig. 2 considers an object that has two scatterers of length l_1 and l_2 along the $\mathbf{RT}_{\perp 2}$ axis. In this diagram, the Doppler generating axis of rotation $\mathbf{\Omega}_{\mathrm{eff}}$ is along the $\mathbf{RT}_{\perp 1}$ axis, and the effective rotation rate is given by $\dot{\theta}_{\mathrm{eff},\Lambda t(n)}$. The rotational motion of the object causes the two scatterers to have a nonzero radial velocity with respect to the radar given by v_1 and v_2. Assume that the radar illuminates the two scatterers for a CPTWL of $\Delta T = \sum_{n=1}^{N-1}\Delta t(n)$, where $N-1$ is the number of discrete rotations over the CPI. At the cross-range resolution limit, given by $\Delta r_{\mathrm{c}} = (l_2 - l_1)$, the radial velocities of the

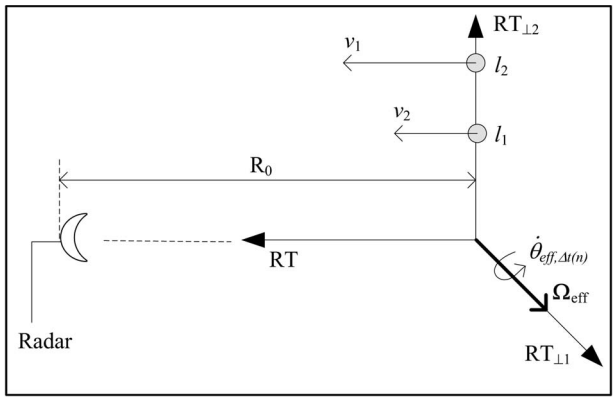

Fig. 2. Diagram used to derive the mathematical expression of the cross-range resolution of an ISAR image.

scatterers are such that their difference in Doppler is equal to the Doppler resolution. Stated mathematically

$$\frac{2v_2}{\lambda} - \frac{2v_1}{\lambda} = \frac{1}{\Delta T}. \tag{26}$$

Rearranging (26) to solve for the cross-range resolution gives

$$\begin{aligned}\frac{2l_2\dot{\theta}_{\mathrm{eff},\Delta t(n)}}{\lambda} - \frac{2l_1\dot{\theta}_{\mathrm{eff},\Delta t(n)}}{\lambda} &= \frac{1}{\Delta T}\\ \frac{2\dot{\theta}_{\mathrm{eff},\Delta t(n)}}{\lambda}(l_1 - l_2) &= \frac{1}{\Delta T}\\ \Rightarrow \Delta r_{\mathrm{c}} &= \frac{\lambda}{2\Delta\theta_{\mathrm{eff}}}\end{aligned} \tag{27}$$

where $\Delta\theta_{\mathrm{eff}} = \sum_{n=1}^{N-1}\dot{\theta}_{\mathrm{eff},\Delta t(n)}\Delta t(n)$ and λ is the wavelength of the transmitted signal. The following assumptions are made about the motion of the object in the mathematical derivation of the cross-range resolution.

1) *Assumption 1:* The Doppler generating axis of rotation does not change with time, and it is aligned to the $\mathbf{RT}_{\perp 1}$ axis throughout the CPI.
2) *Assumption 2:* The effective rotation rate $\dot{\theta}_{\mathrm{eff},\Delta t(n)}$ is constant over the CPI.

Measured motion data of sea vessels have shown that the image-generating Doppler components vary over time [20]. When the motion of the vessel exhibits significant 3-D motion, it fails to satisfy the assumptions that are made in the derivation of the cross-range resolution. As a result, it is inaccurate to apply (27) to transform the cross-range dimension from Doppler to distance. For objects with 3-D rotational motion, it is necessary to relax the assumptions that are made in the derivation of the cross-range resolution. The errors that are made by relaxing these assumptions need to be understood and suitable CPTWL should be chosen to minimize these errors.

A. Relaxing Assumption 1

Consider the case where the Doppler generating axis of rotation $\mathbf{\Omega}_{\mathrm{eff}}$ is not aligned to the $\mathbf{RT}_{\perp 1}$ axis, as shown in Fig. 3. Scatterer 1 and scatterer 2 are located at lengths l_1 and l_2 along the $\mathbf{RT}_{\perp 2}$ axis, respectively. Since $\mathbf{\Omega}_{\mathrm{eff}}$ is offset from the $\mathbf{RT}_{\perp 1}$ axis by an angle of $\theta_{\Omega\mathrm{eff}1}$, the two scatterers appear along the cross-range axis at distances of $l_1\cos(\theta_{\Omega\mathrm{eff}1})$ and $l_2\cos(\theta_{\Omega\mathrm{eff}1})$. The cross-range resolution that is required

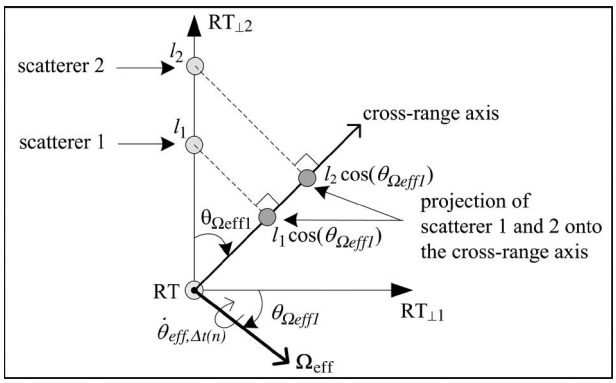

Fig. 3. Diagram illustrating the error in the predicted cross-range resolution when the Doppler generating axis of rotation is not aligned to $\mathbf{RT}_{\perp 1}$ for side-view ISAR imaging.

to separate scatterer 1 and scatterer 2 into two different cross-range bins for a CPTWL of ΔT is given by

$$\frac{2l_2\dot{\theta}_{\mathrm{eff},\Delta t(n)}\cos(\theta_{\Omega\mathrm{eff}1})}{\lambda}-\frac{2l_1\dot{\theta}_{\mathrm{eff},\Delta t(n)}\cos(\theta_{\Omega\mathrm{eff}1})}{\lambda}=\frac{1}{\Delta T}$$
$$\Rightarrow\ \Delta r_{\mathrm{c}1}=\frac{\lambda}{2\Delta\theta_{\mathrm{eff}}\cos(\theta_{\Omega\mathrm{eff}1})}. \tag{28}$$

The cross-range resolution error e_Ω that is made by assuming that $\mathbf{\Omega}_{\mathrm{eff}}$ was aligned to the $\mathbf{RT}_{\perp 1}$ axis is given by

$$e_\Omega=\frac{\Delta r_{\mathrm{c}1}-\Delta r_{\mathrm{c}}}{\Delta r_{\mathrm{c}1}}$$
$$e_\Omega=\frac{\Delta r_{\mathrm{c}1}-\Delta r_{\mathrm{c}1}|\cos(\theta_{\Omega\mathrm{eff}1})|}{\Delta r_{\mathrm{c}1}}$$
$$e_\Omega=1-|\cos(\theta_{\Omega\mathrm{eff}1})|. \tag{29}$$

For objects that possess 3-D rotational motion, the angle of the Doppler generating axis of rotation changes over the CPI. In this case, the maximum cross-range resolution error e_Ω that is made over the CPI is given by

$$e_\Omega=\max_{n\in\{1,N-1\}}\left(1-\left|\cos(\theta_{\Omega\mathrm{eff}1,\Delta t(n)})\right|\right). \tag{30}$$

B. Relaxing Assumption 2

The formula of the cross-range resolution in (27) assumes that the angular rotation rate of the object $\dot{\theta}_{\mathrm{eff},\Delta t(n)}$ is constant over the CPI. In this case, the cross-range resolution Δr_{c} may written in terms of the change in the object's aspect angle over the CPI, denoted by $\Delta\theta_{\mathrm{eff}}$. When $\dot{\theta}_{\mathrm{eff},\Delta t(n)}$ varies over the CPI, it causes the Doppler frequency of a scatterer to migrate through Doppler bins in the ISAR image. For example, consider the system model shown in Fig. 2 that has a time-varying effective angular rotation rate. The scatterer located at length l_1 experiences $d_{\mathrm{b},1}$ Doppler bins of migration, given by

$$d_{\mathrm{b},1}=\max_{n\in\{1,N-1\}}\left(\frac{2l_1\dot{\theta}_{\mathrm{eff},\Delta t(n)}}{\lambda}\right)\Delta T-\min_{n\in\{1,N-1\}}\left(\frac{2l_1\dot{\theta}_{\mathrm{eff},\Delta t(n)}}{\lambda}\right)\Delta T. \tag{31}$$

If d_{b} Doppler bins of migration is allowed in the ISAR image, (31) can be rearranged to express the allowable change in the effective angular rotation rate, denoted by $\Delta\dot{\theta}_{\mathrm{eff}}$, over the CPI

$$\underbrace{\left(\max_{n\in\{1,N-1\}}(\dot{\theta}_{\mathrm{eff},\Delta t(n)})-\min_{n\in\{1,N-1\}}(\dot{\theta}_{\mathrm{eff},\Delta t(n)})\right)}_{\Delta\dot{\theta}_{\mathrm{eff}}}=\frac{\lambda d_{\mathrm{b}}}{2l_{\mathrm{cr}}\Delta T} \tag{32}$$

where l_{cr} is the cross-range extent of the object. It can be observed from (32) that $\Delta\dot{\theta}_{\mathrm{eff}}$ is inversely proportional to the cross-range extent of the object l_{cr}. Thus, for the same λ and ΔT, if l_{cr} increases, the variation in the effective angular rotation rate $\Delta\dot{\theta}_{\mathrm{eff}}$ needs to decrease by the same factor in order for d_{b} to remain the same. This has an impact on ISAR imaging of sea vessels, since the scatterer that experiences the most migration is located at the maximum cross-range extent of the vessel. This corresponds to the height of the tallest mast for the side-view ISAR imaging case. Therefore, the variation of the effective angular rotation rate needs to be smaller for vessels with longer masts for the same allowable Doppler bins of migration.

V. Motion-Aided CPTWL Selection Algorithm

The first step of the proposed MACS algorithm involves the extraction of the image-generating Doppler components from measured motion data (see Section III). Thereafter, the MACS algorithm uses the image-generating Doppler components to select suitable CPTWL for the ISAR imaging process. In this paper, a suitable CPTWL is defined as a processing length that may be applied to a specific radar data set in order to obtain motion-compensated ISAR image(s) with limited blurring due to 3-D motion. In addition, the ISAR image(s) should have the desired cross-range resolution with an acceptable error e_Ω as explained in Section IV.

The MACS algorithm is made up of the following processing steps.

1) Specify appropriate values for the allowable cross-range resolution error, denoted by e_Ω, and the allowable number of Doppler bins of migration, expressed as d_{b}. Thereafter, specify a set of CPTWLs to be evaluated, an overlap factor between two successive CPIs and the desired cross-range resolution Δr_{cd}. Begin the algorithm with the initial value of the CPTWL range.
2) Apply the quaternion-based transformation described in Section III to a vessel's measured motion data in order to extract its image-generating Doppler components.
3) For each CPI, using (30), calculate the cross-range resolution error e_Ω that is made due to the time-varying Doppler generating axis of rotation. In addition, using (31), calculate the maximum Doppler bins of migration d_{b} caused by nonuniform rotation where l_1 corresponds to the maximum cross-range extent. In the side-view ISAR imaging case, if k represents a scatterer at the top of the tallest mast and $t(n)$ is the average absolute time of the CPI, then l_1 is equal to the global coordinates of the kth scatterer given by $w_{k,t(n)}$.
4) If e_Ω and d_{b} is less than that allowed in Step 1), then a suitable CPI has been found. Calculate the cross-range resolution using (27), and if it is better than the desired

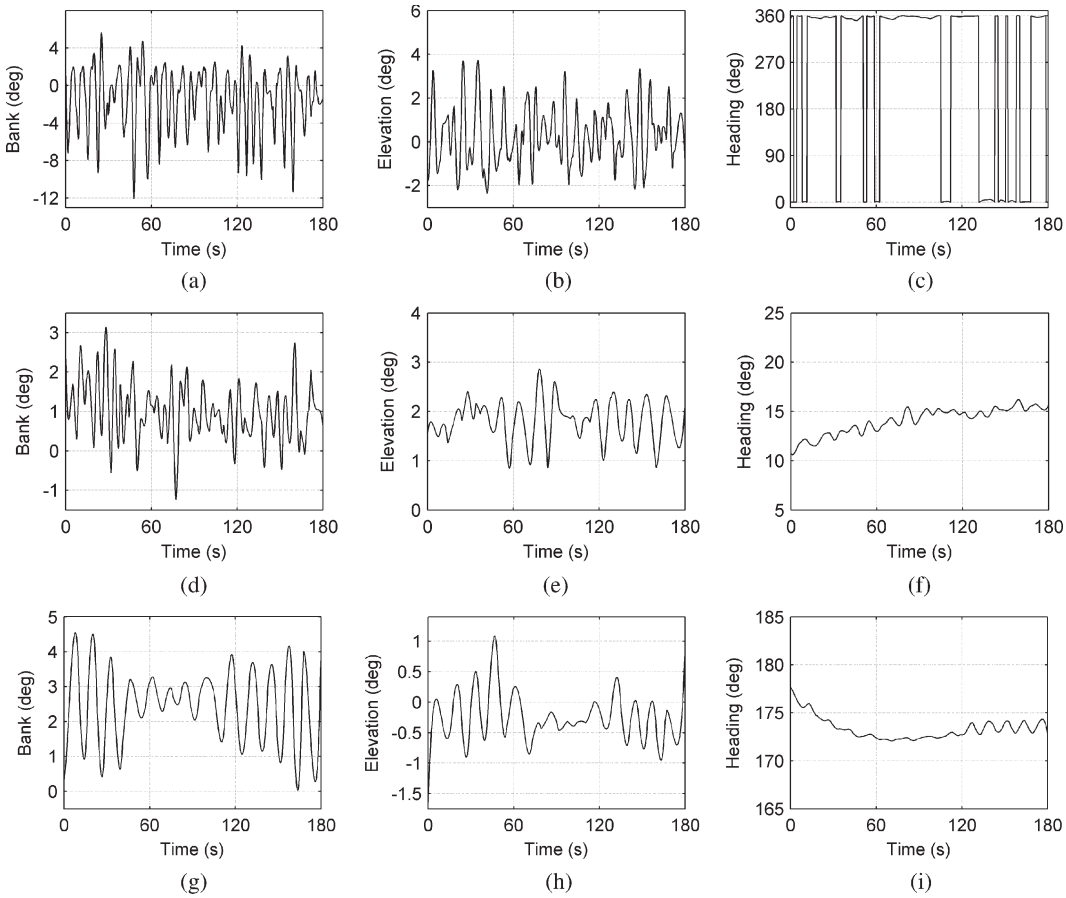

Fig. 4. Measured 3-D rotational motion of (a)–(c) the yacht, (d)–(f) fishing trawler, and (g)–(i) survey vessel.

cross-range resolution, then a suitable CPTWL has been found.

5) Choose the next value in the CPTWL range and if the maximum value has not been reached, go back to Step 2). Otherwise, the algorithm is terminated.

The range of CPTWLs that are chosen in Step 1) is dependent on the vessel of interest, and the next section provides guidelines for three different classes of vessels. If the chosen CPTWL range is not appropriate to a specific data set, it should be changed by the user until a satisfactory result is obtained.

VI. Results

This section presents results from applying the proposed MACS algorithm to measured motion data of three different classes of sea vessels: a yacht, a fishing trawler, and a survey vessel with a weight of 25, 450, and 2750 tons, a length of 20, 60, and 80 m, and a maximum mast height of 15, 20, and 25 m, respectively. Suitable CPTWLs are suggested for each type of vessel. The effectiveness of the suggested CPTWL is demonstrated using measured radar data.

The measured data that are used in this paper were obtained from an ISAR measurement campaign performed in Cape Town, South Africa, during November 2007. All three vessels were instrumented with the Thales ADU5 4-GPS antenna system which measured each vessel's absolute GPS position, heading, elevation, and bank. An experimental X-band radar with a stepped frequency capability was used to obtain radar measurements of the vessels for ISAR imaging purposes. Radar measurements of a sphere suspended from a helicopter was used to compensate the HRR profiles of the yacht for the radar's nonideal response over the stepped frequency band.

TABLE I
Values of the Parameters Used in the MACS Algorithm

Parameter	Value
e_Ω	$\{1\%,\ 5\%,\ 10\%\}$
d_b	$\{2, 3, 4\}$
ΔT (yacht)	$\{0.10s,\ 0.25s,\ \cdots,\ 1.15s\}$
ΔT (fishing trawler)	$\{0.2s,\ 0.4s,\ \cdots,\ 2.4s\}$
ΔT (survey vessel)	$\{0.2s,\ 0.4s,\ \cdots,\ 2.8s\}$
overlap factor	0.75
Δr_{cd} (yacht)	0.75m
Δr_{cd} (fishing trawler)	1m
Δr_{cd} (survey vessel)	1.5m

A. Selection of Suitable CPTWLs

The proposed MACS algorithm was applied to measured motion data of three vessels from different classes. The measured rotational motion of the three vessels is shown in Fig. 4. Each of these recordings is 3 min in duration. The heading measurements indicate that the sailing profile of the yacht and the fishing trawler is inbound, whereas the survey vessel is sailing outbound with respect to the radar. In all three cases,

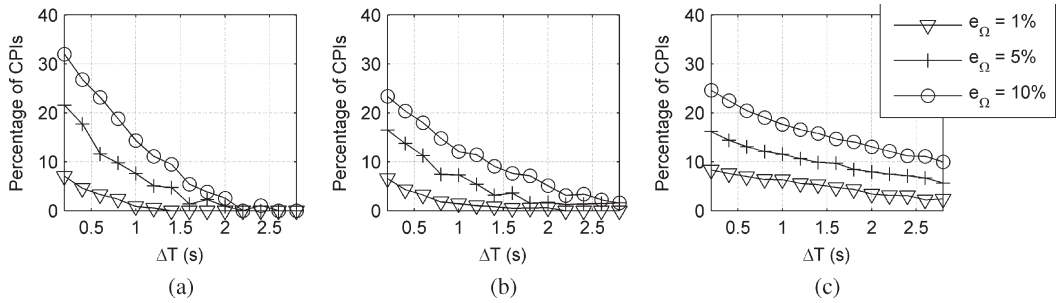

Fig. 5. Diagram showing the effect of the CPTWL ΔT on the percentage of CPIs for various allowable errors e_Ω for (a) the yacht, (b) fishing trawler, and (c) survey vessel.

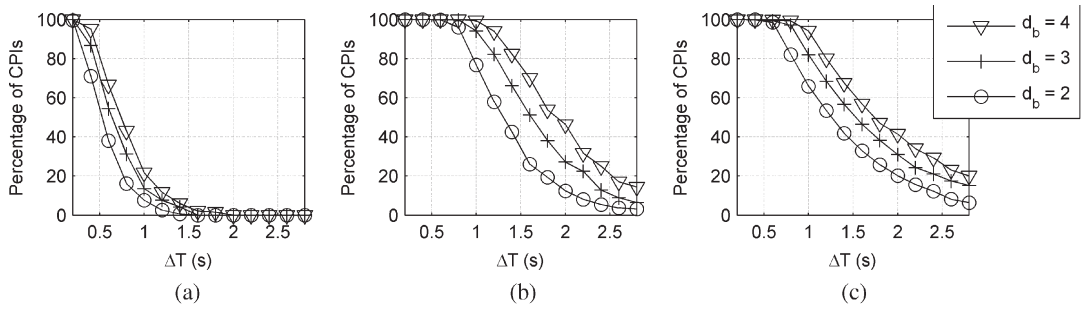

Fig. 6. Diagram showing the effect of the CPTWL ΔT on the percentage of CPIs for various allowable Doppler bins of migration d_{b} for (a) the yacht, (b) fishing trawler, and (c) survey vessel.

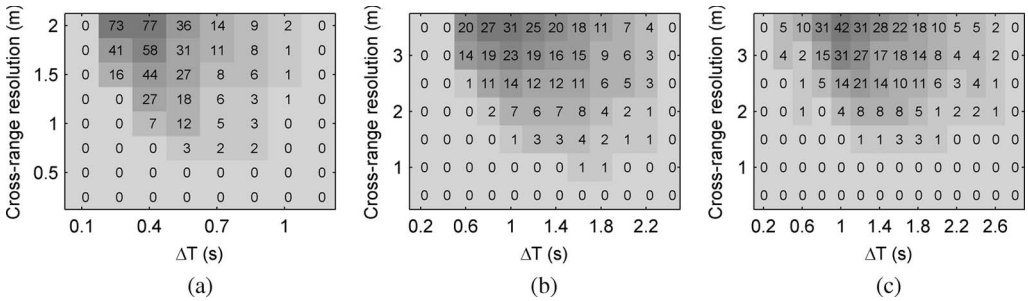

Fig. 7. Diagram showing the histogram of the number of suitable CPIs and their respective cross-range resolution as a function of the CPTWL ΔT for (a) the yacht, (b) fishing trawler, and (c) survey vessel.

the pitch motion of the vessels is used to obtain a side-view ISAR image. The measurements show that the vessels also possess roll and pitch motion as indicated by their bank and elevation angles, respectively, and this causes each vessel's image-generating Doppler components to change with time. In addition, the period of the bank and elevation motion is observed to be longer for heavier vessels. Thus, for larger vessels, the 3-D rotational motion is less chaotic, and it is hypothesized that longer CPTWLs may be accommodated for larger vessels than for smaller vessels.

The proposed MACS algorithm was applied to the measured motion data sets shown in Fig. 4 using the parameter values given in Table I. Figs. 5 and 6 show the effect of the CPTWL on the percentage of CPIs for varying e_Ω and d_{b}, respectively. The percentage of CPIs is given by the percentage of the number of suitable CPIs that are found over the total number of CPIs for a specific CPTWL. It is mathematically expressed as

$$\text{Percentage of CPIs} = \frac{\text{Number of suitable CPIs found}}{\text{Total number of CPIs}}. \quad (33)$$

Fig. 8. Photograph of the yacht.

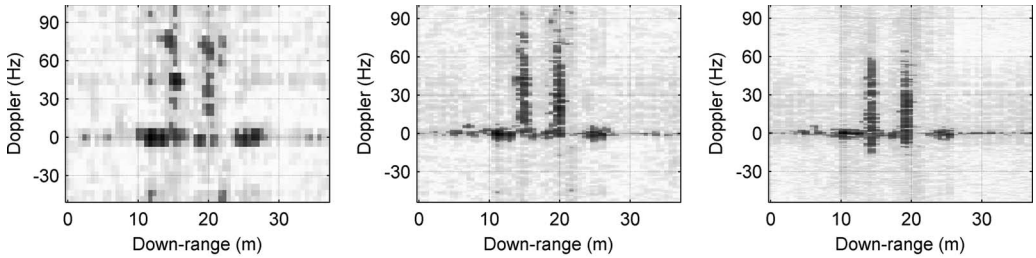

Fig. 9. Motion-compensated ISAR images of the yacht obtained using measured radar data for a CPTWL of (a) 0.2, (b) 0.8, and (c) 1.6 s.

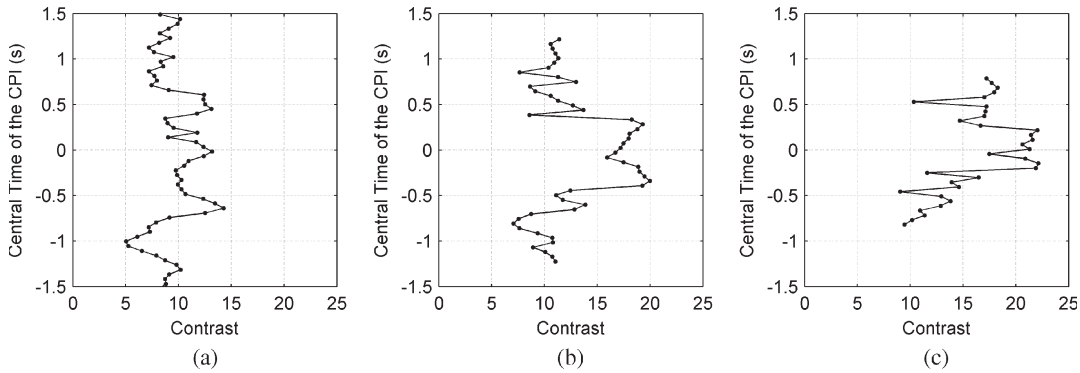

Fig. 10. Image contrast with an initial CPTWL of (a) $\Delta\tau^{(\mathrm{in})} = 0.2$ s, (b) $\Delta\tau^{(\mathrm{in})} = 0.8$ s, and (c) $\Delta\tau^{(\mathrm{in})} = 1.6$ s.

Fig. 5 shows that, as the allowable error e_Ω increases, the percentage of CPIs also increases. This result is expected because, for larger values of e_Ω, the angle of the Doppler generating axis of rotation is allowed to vary by a larger range over the CPI in order for it to be selected as a suitable CPI as indicated by (30). Thus, for larger e_Ω, more suitable CPIs are found, and this causes the percentage of CPIs to increase. Fig. 5 also shows that, as the CPTWL increases, the percentage of CPIs decreases. This outcome is also expected since for longer CPTWL, there are more CPIs that possess significant 3-D rotational motion and fewer CPIs that satisfy the allowable error e_Ω caused by changes in the Doppler generating axis of rotation over the CPI. Similar trends can be observed in Fig. 6, which shows the effects of different allowable Doppler bins of migration d_b and CPTWLs on the percentage of CPIs.

Fig. 7 shows histograms of the number of suitable CPIs that were found for an allowable error of $e_\Omega = 10\%$ and $d_\mathrm{b} = 2$ for each vessel. The histogram shows the cross-range resolution of the suitable CPIs for different CPTWLs. For example, if the CPTWL is chosen to be 1 s for the fishing trawler data set, then Fig. 7(b) shows that there are seven suitable CPIs that have a cross-range resolution of less than or equal to 2 m. These histograms show that for large vessels such as the survey vessel, it is not practical to obtain focused ISAR images with a cross-range resolution of less than 1.5 m for the data set under consideration. On the other hand, for small vessels such as the yacht, the fast pitch motion can be used to obtain focused ISAR images with a cross-range resolution of 0.75 m. These results apply to X-band measurements. One way of improving the cross-range resolution of ISAR images, without changing the motion of a vessel, is to increase the carrier frequency of the radar waveform.

The histograms shown in Fig. 7 are used to select suitable CPTWLs that are able to produce motion-compensated ISAR images with the desired cross-range resolution Δr_cd given in Table I. The achievable cross-range resolution shown in the histograms suggests that suitable CPTWLs for the yacht, the fishing trawler, and the survey vessel are $\{0.55\ \mathrm{s}, 0.85\ \mathrm{s}\}$, $\{1.6\ \mathrm{s}, 1.8\ \mathrm{s}\}$, and $\{1.6\ \mathrm{s}, 2\ \mathrm{s}\}$, respectively. Note that this result confirms the hypothesis that longer CPTWLs may be accommodated for larger vessels in order to obtain motion-compensated ISAR images with the desired medium cross-range resolution.

TABLE II
SUMMARY OF RESULTS OBTAINED FROM APPLYING MARTORELLA/BERIZZI'S ALGORITHM TO A SUBSET OF MEASURED RADAR DATA

Initial CPTWL $\Delta\tau^{(in)}$	Optimum CPTWL $\Delta\tau_{opt}$	Optimum central instant τ_{opt}
0.2s	0.34s	-0.64s
0.8s	0.86s	-0.34s
1.6s	1.64s	-0.15s

The effectiveness of the suggested CPTWL for the yacht was demonstrated using radar data that were measured during the same time period as the motion data set. The radar data set was obtained with an experimental X-band radar that transmitted a stepped frequency waveform with the following radar parameters: a frequency step of 4 MHz, 64 pulses in an ISAR burst, and a burst repetition frequency of 154 Hz. A photograph of the instrumented yacht is shown in Fig. 8. The motion data and the radar data were both time-stamped using a GPS receiver, which made it possible to extract useful radar data corresponding to the absolute time period of a suitable CPI for ISAR imaging purposes. Fig. 9 shows motion-compensated ISAR images of the yacht for three different CPTWLs. Translation motion compensation was achieved using the global range alignment algorithm [9] and the autofocus algorithm proposed

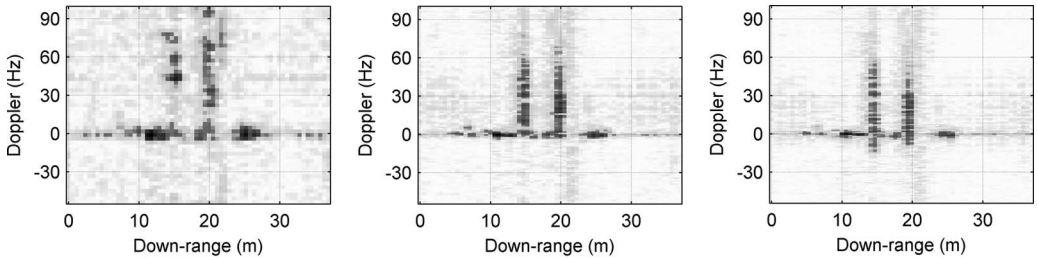

Fig. 11. ISAR images obtain using the optimum imaging parameters of (a) $\Delta\tau_{\rm opt} = 0.34$ s and $\tau_{\rm opt} = -0.64$ s, (b) $\Delta\tau_{\rm opt} = 0.86$ s and $\tau_{\rm opt} = -0.34$ s, and (c) $\Delta\tau_{\rm opt} = 1.6$ s and $\tau_{\rm opt} = -0.15$ s.

by Yuan and Casasent [3]. Fig. 9(a) shows the ISAR image of the yacht for a CPTWL of 0.2 s. The spreaders along the masts of the yacht can be observed; however, the image has a few undesirable characteristics: The cross-range resolution is poor because the change in aspect angle (or pitch motion) over the CPI is too small, the structure of the yacht's two masts is indiscernible, and the front of the yacht is not clearly apparent. In this case, the CPTWL is too short. These limitations are overcome when the CPTWL is increased to 0.8 s, as shown by the ISAR image in Fig. 9(b). It should be noted that the CPTWL of 0.8 s corresponds to that suggested by the proposed MACS algorithm for the yacht data set. Lastly, when the CPTWL is increased further to 1.6 s, it leads to a blurred ISAR image, as shown in Fig. 9(c). In this case, the CPTWL is too long, and blurring is caused by the yacht's 3-D rotational motion.

As described in the previous paragraph, the absolute time of the suitable CPIs with the desired cross-range resolution may be used to extract useful subsets of radar data for ISAR imaging purposes. This can be achieved when the motion data and the radar data are time-stamped using the same time clock. This feature would provide significant computational savings for RCS measurement applications where long radar recordings are made and only a few high-quality ISAR images are required. Lastly, the range of CPTWLs that is suggested by the MACS algorithm can be used to select a high-quality initial CPTWL for optimum imaging selection algorithms that operate on measured radar data. The value of using the suggested CPTWLs to choose an effective initial CPTWL value for Martorella/Berizzi's optimum imaging selection algorithm in [18] is demonstrated in the next section.

B. Effectiveness of the Suggested CPTWLs for Martorella/Berizzi's Algorithm

The MACS algorithm uses measured motion data to suggest a range of CPTWLs that is suitable for ISAR imaging. A range of CPTWLs is suggested after assessing a range of discrete values. An improved CPTWL can be obtained using Martorella/Berizzi's optimum imaging selection algorithm that operates on measured radar data. This algorithm uses the contrast of the measured ISAR images to select the optimum imaging parameters for a particular radar data set. Martorella/Berizzi's algorithm was applied to the measured radar data set with a sliding window of eight HRR profiles and an initial window length increase, denoted as "2n" in [18], of 12 HRR profiles. The results obtained for three different initial CPTWLs, denoted by $\Delta\tau^{(\rm in)}$, is shown in Fig. 10 and Table II.

Fig. 10 shows that the image contrast of the ISAR images is dependent on the value of the initial CPTWL $\Delta\tau^{(\rm in)}$. The dependence of the absolute value of the image contrast on $\Delta\tau^{(\rm in)}$ was reported in [18]. Furthermore, results in [18] show that the choice of $\Delta\tau^{(\rm in)}$ does not affect the central instant of the CPTWL, denoted by $\tau_{\rm opt}$, for large vessels. However, results in Table II clearly show that the optimum central instant $\tau_{\rm opt}$ is dependent on the initial value of the CPTWL, for small vessels. In addition, the optimum CPTWL $\Delta\tau_{\rm opt}$ is different for each initial CPTWL of $\Delta\tau^{(\rm in)}$. It should be noted that the authors of [18] clearly mention that their proposed algorithm has not been tested on small ships, as this represented future work.

The optimum imaging parameters, which is given in Table II, was applied to the radar data set and the ISAR images that were obtained is shown in Fig. 11. The ISAR images shown in Fig. 11 are very similar to the images shown in Fig. 9. Thus, the comments that were made about Fig. 9 applies to the Fig. 11 as well. It should be noted that it is only Fig. 11(b) that shows an image of yacht with two equally long masts. Moreover, the optimum CPTWL of 0.86 s was obtained using a good quality initial CPTWL value of $\Delta\tau^{(\rm in)} = 0.8$ s, which was selected from the range of CPTWLs suggested by the MACS algorithm. This demonstrates the value of the MACS algorithm in providing a good quality initial CPTWL for Martorella/Berizzi's optimum imaging selection algorithm when it is applied to radar measurements of small vessels.

VII. Conclusion

This paper presented a new technique, referred to as the MACS algorithm, which is used to select suitable CPTWLs for ISAR imaging of cooperative sea vessels. The proposed algorithm uses measured motion data of an instrumented vessel to extract the image-generating Doppler components, which consists of the Doppler generating axis of rotation and effective angular rotation rate. Thereafter, the MACS algorithm uses the image-generating Doppler components to suggest suitable CPTWLs that may be used to obtain motion-compensated ISAR images with limited blurring due to 3-D rotational motion. Furthermore, these suggested CPTWLs minimize the error in the predicted cross-range resolution due to changes in the Doppler generating axis of rotation over the CPI. The MACS algorithm was applied to motion data sets of three different classes of sea vessels: a yacht, a fishing trawler, and a survey vessel. The suggested CPTWLs indicate that a longer CPTWL is needed for larger vessels. Experimental results obtained using measured radar data show the effectiveness of the proposed algorithm.

The suggested CPTWL may be used to select an effective initial CPTWL for Martorella/Berizzi's optimum imaging selection algorithm when it is applied to measured radar data of small vessels. When the radar and motion data are time-stamped using the same time clock, the proposed MACS algorithm may be used to extract subsets of radar data which are useful for ISAR imaging purposes. In this way, significant computational savings may be achieved for RCS measurement applications, where long radar recordings are made and only a few high-quality ISAR images are required.

ACKNOWLEDGMENT

The authors would like to thank K. Naicker for his work on the calibration of the measured HRR profiles. The authors would also like to thank J. Cilliers, A. le Roux, F. Anderson, and Prof. C. J. Baker for their technical inputs and to members of the Council for Scientific and Industrial Research's Radar and Electronic Warfare team who were involved with the radar measurements.

REFERENCES

[1] A. Jain and I. Patel, "Dynamic imaging and RCS measurements of aircrafts," *IEEE Trans. Aerosp. Electron. Syst.*, vol. 31, no. 1, pp. 211–226, Jan. 1995.

[2] S. Musman, D. Kerr, and C. Bachmann, "Automatic recognition of ISAR ship images," *IEEE Trans. Aerosp. Electron. Syst.*, vol. 32, no. 4, pp. 1392–1404, Oct. 1996.

[3] C. Yuan and D. Casasent, "Composite filters for inverse synthetic aperture radar," *Proc. SPIE*, vol. 41, pp. 94–104, Jan. 2002.

[4] M. Martorella, N. Acito, and F. Berizzi, "Statistical clean technique for ISAR imaging," *IEEE Trans. Geosci. Remote Sens.*, vol. 45, no. 11, pp. 3552–3560, Nov. 2007.

[5] D. R. Wehner, *High-Resolution Radar*, 2nd ed. Norwood, MA: Artech House, 1995.

[6] V. C. Chen and W. J. Miceli, "Simulation of ISAR imaging of moving targets," *Proc. Inst. Elect. Eng.—Radar, Sonar Navig.*, vol. 148, no. 3, pp. 160–166, Jun. 2001.

[7] V. Chen and R. Lipps, "ISAR imaging of small craft with roll, pitch and yaw analysis," in *IEEE Int. Radar Conf. Rec.*, May 7–12, 2000, pp. 493–498.

[8] Z. Bao, G. Wang, and L. Luo, "Inverse synthetic aperture radar imaging of maneuvering targets," *Opt. Eng.*, vol. 37, no. 5, pp. 1582–1588, May 1998.

[9] J. Wang and D. Kasilingam, "Global range alignment for ISAR," *IEEE Trans. Aerosp. Electron. Syst.*, vol. 39, no. 1, pp. 351–357, Jan. 2003.

[10] B. Haywood and R. J. Evans, "Motion compensation for ISAR imaging," in *Proc. Australian Symp. Signal Process. Appl.*, Adelaide, Australia, 1989, pp. 112–117.

[11] J. M. Munoz-Ferreras and F. Perez-Martinez, "Extended envelope correlation for range bin alignment in ISAR," in *Proc. IET Radar Conf.*, Oct. 2007, pp. 1–5. session 2d, No. 1.

[12] D. E. Wahl, P. H. Eihel, D. C. Ghiglia, and C. V. Jakowatz, Jr., "Phase gradient autofocus a robust tool for high resolution SAR phase correction," *IEEE Trans. Aerosp. Electron. Syst.*, vol. 30, no. 3, pp. 827–834, Jul. 1994.

[13] B. D. Steinberg, "Microwave imaging of aircraft," *Proc. IEEE*, vol. 76, no. 12, pp. 1578–1988, Dec. 1989.

[14] J. M. Munoz-Ferreras and F. Perez-Martinez, "Uniform rotational motion compensation for inverse synthetic aperture radar with noncooperative targets," *Proc. Inst. Elect. Eng.—Radar, Sonar Navig.*, vol. 2, no. 1, pp. 25–34, Feb. 2008.

[15] G. Y. Lu and Z. Bao, "Compensation of scatterer migration through resolution cell in inverse synthetic aperture radar imaging," *Proc. Inst. Elect. Eng.—Radar, Sonar Navig.*, vol. 147, no. 2, pp. 80–85, Apr. 2000.

[16] M. Martorella, "Novel approach for ISAR image cross-range scaling," *IEEE Trans. Aerosp. Electron. Syst.*, vol. 44, no. 1, pp. 281–294, Jan. 2008.

[17] M. Y. Abdul Gaffar and W. A. J. Nel, "Investigating the effect of a target's time-varying Doppler generating axis of rotation on ISAR image distortion," in *Proc. IET Radar Conf.*, Oct. 2007, pp. 1–5. session 5b, No. 4.

[18] M. Martorella and F. Berizzi, "Time windowing for highly focused ISAR image reconstruction," *IEEE Trans. Aerosp. Electron. Syst.*, vol. 41, no. 3, pp. 992–1007, Jul. 2005.

[19] J. Kuipers, *Quaternions and Rotation Sequences: A Primer with Applications to Orbits, Aerospace and Virtual Reality*. Princeton, NJ: Princeton Univ. Press, 1999.

[20] M. Y. Abdul Gaffar, W. A. J. Nel, and M. R. Inggs, "Quaternion-based transformation for extraction of image-generating Doppler for ISAR," *IEEE Geosci. Remote Sens. Lett.*, vol. 5, no. 4, pp. 560–563, Oct. 2008.

[21] S. Wong, G. Duff, and E. Riseborough, "ISAR image distortion due to small perturbed motion and restoration of distorted images by time–frequency analysis," *Proc. SPIE*, vol. 5102, pp. 200–212, Apr. 2003.

M. Y. Abdul Gaffar received the B.Sc.Eng. (Electronic) and M.Sc.Eng. (Electronic) degrees in electronic engineering from the University of Natal, Natal, South Africa, in 2002 and 2003, respectively. Since 2006, he has been working toward the Ph.D. degree in electrical engineering at the University of Cape Town, Rondebosch, South Africa, focusing on the field of inverse synthetic aperture radar (ISAR) imaging of sea vessels with 3-D rotational motion.

In 2004, he joined the Radar and Electronic Warfare Competence at the Council for Scientific and Industrial Research, where he worked on propagation modeling and inverse synthetic aperture radar imaging of aircraft. His research interests include motion compensation of ISAR images and ISAR-based classification of noncooperative objects.

W. A. J. Nel received the B.Sc.Eng. (Electronic) degree in electronic engineering from the University of Pretoria, Pretoria, South Africa, in 1996 and the M.Sc.Eng. (Electronic) degree in digital image processing from the University of Cape Town, Rondebosch, South Africa, in 1998.

Since 1999, he has been with the Radar and Electronic Warfare (EW) Research Competence at the Council for Scientific and Industrial Research (CSIR), Pretoria, where he is currently a Principal Researcher in the area of radar target recognition and radar signal processing. He is also involved in the technology management of the Radar/EW research group. During his career at CSIR, he has been involved in many areas of radar and EW research and has a strong background in the fields of radar signal processing, synthetic aperture radar (SAR)/inverse SAR, high range resolution, and radar target recognition.

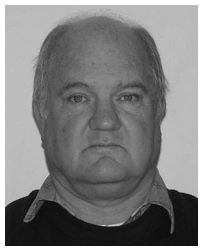

M. R. Inggs received the B.Sc. (Hons.) degree in physics and applied mathematics from Rhodes University, Grahamstown, South Africa, in 1973 and the Ph.D. degree from Imperial College, London University, London, U.K., in 1979.

He was with the South Africa Naval Dockyard (Simon's Town), ESD (Halfway House), which is currently known as Reutech Radar Systems (RRS), Raytheon Data Systems (Norwood, MA), RF Technology Centre (Leatherhead, U.K.), Imperial College, and Decca Radar Research Laboratories (Hersham, U.K.). His work has concentrated on radar systems, microwave components, and signal processing applied to radar and communications. Since 1988, he has been a Professor with the Department of Electrical Engineering, University of Cape Town, Rondebosch, South Africa. Currently, he supervises many groups of postgraduate students working in the fields of radar and reconfigurable high-performance computing. He holds a joint appointment with the Centre for High Performance Computing, Rosebank, South Africa.